



Core-shell VO₂@TiO₂ nanorods that combine thermochromic and photocatalytic properties for application as energy-saving smart coatings

Yamei Li¹, Shidong Ji¹, Yanfeng Gao^{1,2}, Hongjie Luo^{1,2} & Minoru Kanehira¹

¹State Key Laboratory of High Performance Ceramics and Superfine Microstructure, Shanghai Institute of Ceramics, Chinese Academy of Sciences, Dingxi 1295, Changning, Shanghai, 200050, China, ²School of Materials Science and Engineering, Shanghai University, Shangda Rd. 99, Baoshan, Shanghai 200444, China.

Vanadium dioxide (VO₂) is a Mott phase transition compound that can be applied as a thermochromic smart material for energy saving and comfort, and titanium dioxide (TiO₂) is a well-known photocatalyst for self-cleaning coatings. In this paper, we report a VO₂@TiO₂ core-shell structure, in which the VO₂ nanorod core exhibits a remarkable modulation ability for solar infrared light, and the TiO₂ anatase shell exhibits significant photocatalytic degradation of organic dye. In addition, the TiO₂ overcoating not only increased the luminous transmittance of VO₂ based on an antireflection effect, but also modified the intrinsic colour of VO₂ films from yellow to light blue. The TiO₂ also enhanced the chemical stability of VO₂ against oxidation. This is the first report of such a single nanoparticle structure with both thermochromic and photocatalytic properties that offer significant potential for creating a multifunctional smart coating.

The world's available energy resources have been diminishing since the beginning of the 21st century, and saving energy is one of the most effective ways to solve this energy shortage problem. It is estimated that buildings are responsible for more than 40% of primary energy use in most countries¹, primarily for space heating and cooling for indoor comfort. Energy-efficient wall or window coatings are considered to be the first step for reducing heat transfer between the indoor and outside environments. Energy efficient commercial products have already been developed, such as the Low-E window that possesses a low emissivity to achieve high thermal reflectivity of infrared light. Although the Low-E window has been widely used in the building industry, one of its disadvantages is that it cannot change its optical properties in response to environmental temperature changes or different human needs². Based on the metal-to-semiconductor phase transition (MST, Fig. 1), vanadium dioxide (VO₂) smart windows can exhibit automatic solar/heat control in response to environmental temperatures without the use of any external switching device, in comparison with other chromogenic windows, such as electrochromic or gasochromic, and it has recently attracted considerable attention. VO₂ undergoes a reversible MST at ~68°C, that is accompanied by a structural phase transition from monoclinic (P2₁/c, M1 phase) to tetragonal (P4₂/mnm, R phase) symmetry with an abrupt change in optical properties from transmitting to highly reflecting particularly in the infrared spectral region^{3,4}. Thermochromic coatings have recently been developed using physical or chemical vapour deposition (e.g., sputtering⁵ or CVD⁶), polymer-assisted deposition^{7–10} and flexible foils by soft chemical methods^{11,12}, and some prototype products have also been produced by our research group^{11,13}.

Furthermore, environmental pollution as a by-product of rapid industrial development is another serious problem in addition to the energy shortage. Air quality is worsening in large cities, and consequently, for example, the windows/walls of buildings are becoming dirtier more easily and require more frequent, labour-intensive cleanings that require extra organic detergents which cause secondary contamination. It is known that photocatalysts are effective for the degradation of organic dirt compared to the use of detergents. Among the various types of photocatalysts, titania (TiO₂) is the most suitable material because of its excellent photocatalytic degradation ability for organic pollutants and photo-induced hydrophilicity¹⁴.

From the above background discussion, it is hypothesised that a composite material with a combination of VO₂ and TiO₂ would present both energy-efficiency and environmental protection properties. This proposed

SUBJECT AREAS:
PHOTOCATALYSIS
CHEMICAL ENGINEERING
ENVIRONMENTAL CHEMISTRY
OPTICAL MATERIALS

Received
13 November 2012

Accepted
17 January 2013

Published
2 April 2013

Correspondence and requests for materials should be addressed to Y.F.G. (yfgao@shu.edu.cn) or M.K. (p-jin@mail.sic.ac.cn)

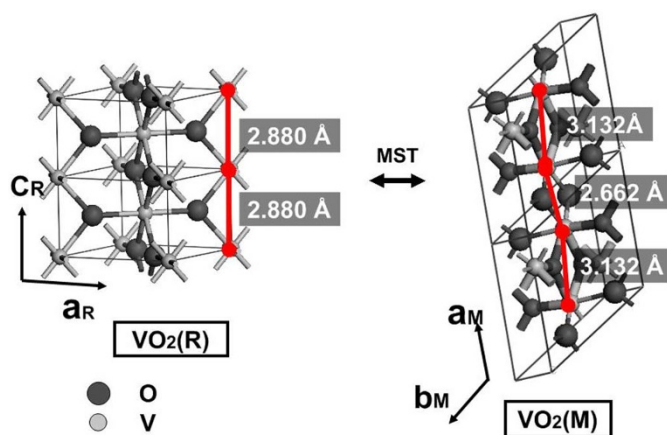


Figure 1 | The crystallographic structure of $\text{VO}_2(\text{M1})$ and $\text{VO}_2(\text{R})$. After metal-to-semiconductor transition (MST), linear and equal-distant (2.880\AA) V-V chains along C_R axis in tetragonal R phase become distorted with alternative distances at 3.132\AA and 2.662\AA with unit cell doubled in monoclinic M phase. Such a structural transition was accompanied with a small volumetric change of 0.044% .

composite is a thrilling concept and of great value for applications in functional films/coatings. In fact, a multilayer structure of $\text{TiO}_2/\text{VO}_2/\text{glass}$ deposited using PVD^{15,16} (magnetron sputtering) and a VO_2/TiO_2 (anatase) composite film deposited using APCVD^{6,17} have been proposed for smart window applications; however, the above deposition processes are either expensive or hardly demonstrate photocatalytic performance.

A series of studies by our group^{11,18} have demonstrated that a nanopowder-based solution coating process may likely be a superior alternative to the PVD or CVD methods because of some advantages including simple coating systems, flexibility for substrate selection, ease for large-scale production and low-cost. Note that such functional plastic foils are considerably more suitable for windows on vehicles and old buildings; the latter represents a very large market. Because of the polymorphism of VO_2 and the metastable valence of vanadium¹⁹, controlling the synthesis of VO_2 mono-dispersed particles with a pure crystalline phase and a uniform morphology has long been a challenge. The majority of the developed methods can only produce either B/A metastable phases or M1/R phases with non-uniform morphologies²⁰. Fortunately, there have recently been exciting breakthroughs in the synthesis of VO_2 mono-dispersed single phase nanopowders by the hydrothermal method^{12,18,21–23}. These technologies make it possible to achieve flexible foils.

The high chemical stability, the modified colour of VO_2 film, and a narrow hysteresis are three key requirements for VO_2 thermochromic coatings. However, VO_2 is gradually oxidised into toxic V_2O_5 in wet ambient atmospheres²⁴, which leads to a considerable deterioration of its thermochromic properties. Enhancing the chemical stability of VO_2 against oxidation is urgently required. VO_2 films with grain size below 600 nm usually hold a yellowish colour, which originates from visible absorption specially in the $\sim 300\text{--}400\text{ nm}$ region⁹. Reducing the yellow colour or changing to more acceptable colours favours applications for VO_2 . Hysteresis problem is rarely considered in powder-based films at present, however in principle, $20\text{--}26^\circ\text{C}$ is considered to be a favorable temperature range for human comfort, so hysteresis higher than $\sim 6^\circ\text{C}$ will be inappropriate for real applications. However, films prepared using powders in reported studies commonly exhibited a very wide hysteresis^{9,10}. For smart coatings deposited by PVD, it has been reported that a TiO_2 layer coated on a VO_2 film enhanced the luminous transmittance through an anti-reflecting (AR) effect, which may also likely protect the VO_2 film against oxidation^{15,16}.

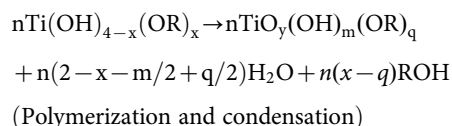
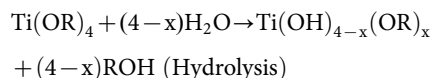
Similarly in the case of nanopowders, core/shell nanotechnology is an available and facile method to obtain multifunctional VO_2/TiO_2 powders. Some pioneering works using VO_2 as a core for the formation of core-shell composites have been reported. Jin, P.²⁵ and Gao, Y. F. et al¹¹ prepared VO_2/SiO_2 core-shell nanoparticles, and Gao successfully made them into flexible foils with excellent solar energy modulation abilities and highly enhanced chemical stability. Although TiO_2 exhibits advantages over SiO_2 because of its photocatalytic properties, there are no reports on the production of high performance VO_2/TiO_2 composite nanopowders with both thermochromic and photocatalytic properties and a high chemical stability.

In this paper, we report for the first time synthesis of novel VO_2/TiO_2 core/shell nanoparticles using the consecutive hydrothermal synthesis of VO_2 , the sol-gel to prepare the titania precursor coating and a strictly controlled vacuum-annealing for crystallising the titania shell (Fig. 2). The VO_2/TiO_2 core/shell nanoparticles exhibit multiple functions: thermochromism from the VO_2 core for solar energy modulation, photocatalytic properties from the TiO_2 shell for environmental purification, and highly enhanced chemical stability of VO_2 . Furthermore, it was observed that a TiO_2 layer with a proper thickness can increase the visible transmittance of the coating using VO_2/TiO_2 nanoparticles and modify the yellow colour to a more pleasant blue one. Meanwhile, the coated VO_2 showed a narrower hysteresis. The above technique breakthroughs will play a role in obtaining materials with integrated energy-savings and environmental protection functions for building applications.

Results

Formation of core/shell nanostructure. Pure, single crystalline $\text{VO}_2(\text{M1})$ powders were obtained after hydrothermal treatment. Fig. 3 presents the SEM, TEM images and the XRD pattern of the as-prepared VO_2 nanorods. The SAED pattern in Fig. 3-b demonstrated that the as-prepared VO_2 has a typical preferential growth direction along $[100]$ ($//a\text{M1}$ axis), which is in accordance with previous reports^{12,19}. The as-synthesised VO_2 nanorods have a uniform morphology with an average short diameter of $500\text{--}600\text{ nm}$.

The sol-gel process was used to produce TiO_2 precursor shells with controllable thicknesses (Fig. 2). Detailed experimental parameters for some samples are listed in Table 1. The $\text{Ti}(\text{OR})_4\text{-H}_2\text{O}$ -alcohol ($R = \text{-CH}_3, \text{-C}_2\text{H}_5, \text{-C}_3\text{H}_7, \text{-C}_4\text{H}_9$) system has been used for titania coating in the past decade on both particles^{26,27} and thin films^{28,29}. $\text{Ti}(\text{OR})_4$ is hydrolysed and then peptized into titania colloids by condensation. The general reactions for these two processes are schematically described below:



In this study, a carefully-controlled moderate hydrolysing process was achieved by utilising a relatively low concentration of reagents ($\text{Ti}(\text{OR})_4$ and H_2O). The slow and dropwise addition of the $\text{H}_2\text{O}/\text{ethanol}$ mixture under vigorous stirring is important for nucleating and precipitating hydrolysed species on the VO_2 surface to ensure a homogenous gel coating (Results of comparative experiments with increased concentrations and rapid addition (N6 and N7) are shown in supplementary Fig. S1, and the Tyndall phenomenon was used to determine whether isolated titania species are formed). Previous sol-gel synthesis studies have revealed that the $\text{TBOT-H}_2\text{O-ethanol}$ system with an excessive water content, typically with a $\text{TBOT:H}_2\text{O}$ molar ratio at $1:4$ ³⁰ and $1:220$ ³¹, readily resulted in homogeneous

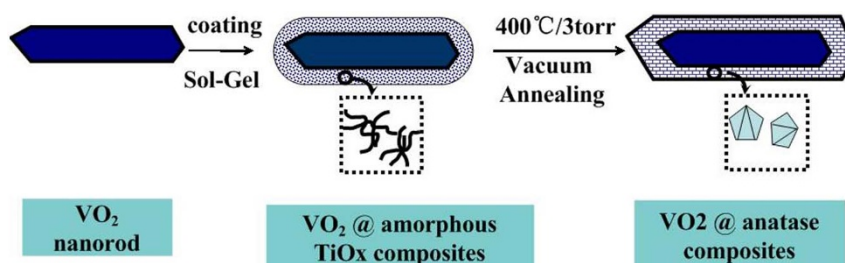


Figure 2 | Illustration of coating and annealing procedures. By sol-gel reaction at 80°C with reflux condenser for 2 h, TBOT was hydrolysed and precipitated onto the surface of VO₂ nanorods and then collected by filtration. Then dried powders were annealed in vacuum quartz tube under proper temperature and pressure with the shell transformed into crystallised TiO₂.

precipitation. In our process, homogeneous precipitation was largely diminished (the filtrate solution did not exhibit the Tyndall effect) by adopting the above mentioned lower concentration of reagents and the slow addition method to avoid a large degree of supersaturation. Therefore, titania species will preferentially precipitate onto the surface of the core VO₂ rods to form shell coatings.

To obtain a crystalline coating, the annealing procedure was carefully investigated because of the ease of oxidation of VO₂ in air or oxygen-rich atmospheres at relatively high temperatures ($\sim 350^\circ\text{C}$)³². The results from TG-DTA measurements (see supplementary Fig. S2) indicate that samples N1 and N2 initially experienced a considerable mass loss until 300–350°C that resulted from the oxidation of organic -OR (R = (CH₂)₃CH₃), which was followed by an abrupt weight gain caused by the oxidation of VO₂. Previous studies have demonstrated that the transition from the amorphous titania gel precursor to anatase commonly begins at approximately $\sim 350^\circ\text{C}$ and a higher temperature, such as $\sim 400^\circ\text{C}$ ^{29,31,33}, favours an increase in crystallinity. Oxygen is essential for the removal of organic species (-OR) in amorphous titania shells, but an excessive amount of O₂ leads to the oxidation of VO₂. The two critical synthesis parameters, annealing temperature (T) and air pressure (P), should be carefully controlled to crystallise titania without oxidising VO₂.

To determine the appropriate annealing parameters, the annealing performance of VO₂ powders was investigated (see supplementary Fig. S3). At temperatures greater than 500°C, pure VO₂ can be oxidised into high-valence vanadium oxides (e.g., V₃O₇ and V₂O₅) at a

rather high pressure (~ 30 torr, an oxygen-rich atmosphere) or change into amorphous or partially reduced states under oxygen-deficient conditions (~ 48 mtorr). Similar results have been reported in the study of the synthesis of a VO₂ film by reduction from V₂O₅³⁴, in which a temperature and pressure-dependent dynamic equilibrium $\text{V}_2\text{O}_5 \leftrightarrow \text{V}_3\text{O}_7 \leftrightarrow \text{V}_4\text{O}_9 \leftrightarrow \text{V}_6\text{O}_{13} \leftrightarrow \text{VO}_2$ between V₂O₅ and its reduced derivatives was revealed. This redox behaviour is a result of the multi-valence nature of the V-O system and a rather narrow solubility range of oxygen in the VO₂ lattice³⁵. This result implies that an appropriate oxidative atmosphere (with a certain proportion of oxygen at an air pressure of 48 mtorr ~ 3 torr) with a proper temperature (400°C $\sim 450^\circ\text{C}$) are preferable for obtaining the crystallisation of titania while keeping the VO₂ core intact.

Based on the above discussion, the four composite samples were annealed (supplementary Fig. S3), and the optimised temperature and air pressure were $\sim 400^\circ\text{C}$ and ~ 3 torr, respectively. All samples under discussion in the following sections of this paper were treated using this same protocol. Fig. 4 presents the XRD patterns of samples N1–N4 before and after annealing. In the VO₂@TiO_x (amorphous gel) samples before annealing (Fig. 4-a), only peaks belonging to VO₂ (JCPDF card No. 82-0661) were detected, which indicates that the gel coatings in all samples are amorphous or poorly crystallised. After annealing, the amorphous gel coatings were crystallised into anatase (JCPDF card No. 21-1272) without changes of the VO₂ crystalline phase. However, the peaks that correspond to titanium oxides were not clearly detected for sample N1 because of a limited thickness, which will be discussed in the following.

Fig. 5 (a) to (d) present the SEM images of the annealed core-shell particles N1–N4 with different thicknesses. Thick coatings (100–200 nm for N3 and N4) contain a considerable amount of apparent cracks that result from the relaxation of thermal stress, which can hardly be observed in the thinner coatings (N1 and N2). By increasing the loading amount of VO₂ (m/g), the mean coating thickness (d/nm) become stably reduced from ~ 200 nm (0.03 g VO₂, sample N4) to ~ 20 nm (0.2 g VO₂, sample N1) with a nearly

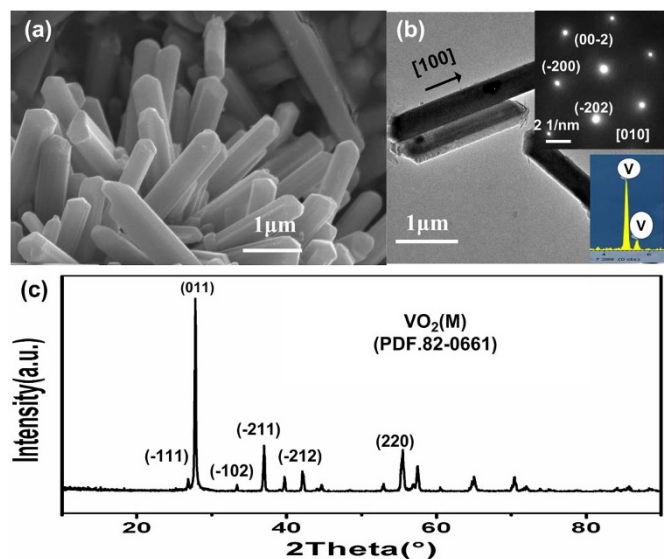


Figure 3 | As-synthesized VO₂ nanorods. (a), (b) and (c) showed the SEM, TEM images and XRD pattern for as-synthesized VO₂ nanorods, respectively. TEM showed a growing direction along $a_{M1} \langle 100 \rangle$.

Table 1 | Experimental parameters for different samples (all at 80°C and react for 2 hours)

Sample number	VO ₂ mass (g)	TBOT volume (mL)	H ₂ O volume (mL) ^a	Coating thickness (nm) ^c
N1	0.25	0.5	20	20
N2	0.1	0.5	20	70
N3	0.07	0.5	20	100
N4	0.03	0.5	20	200
N5	0.2	0.5	20	50
N6	0.1	0.5	20 ^b	-
N7	0.1	1	20	-

^aAmount of H₂O solution (~ 50 mL/L in ethanol) added for 80 mL of suspension.

^b20 mL H₂O with concentration of 100 mL/L in ethanol.

^cCoating thickness were evaluated from TEM and SEM measurements.

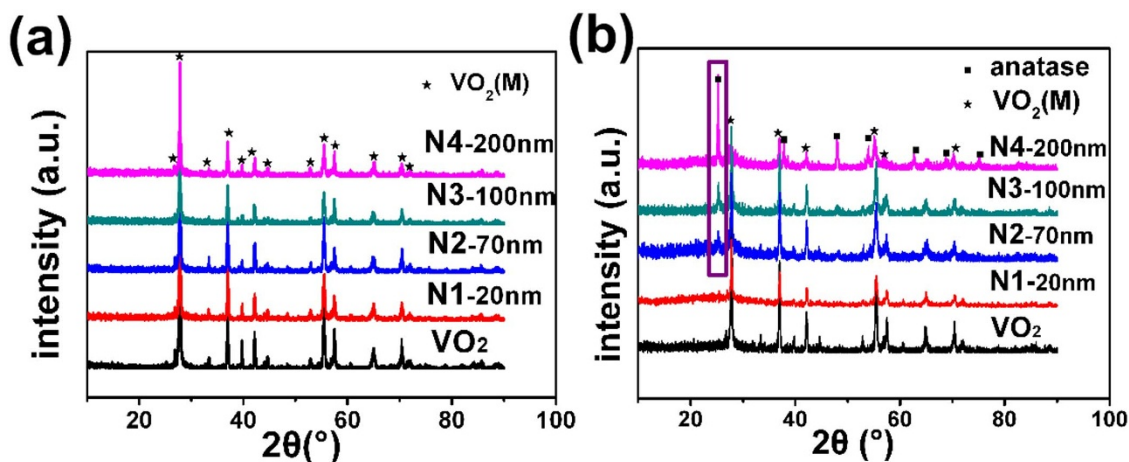


Figure 4 | XRD patterns for pure VO₂ and composite samples (N1 to N4) before (a) and after (b) annealing. Before annealing, only VO₂ can be detected, indicating the shell was amorphous or poorly crystallized. After annealing, peaks ascribing to anatase TiO₂ can be distinguished from pre-existing VO₂ peaks.

inverse proportional d-m relationship (refer to supplementary Fig. S4); this relationship is made possible because the precipitation rate was maintained constant by decreasing the homogeneous precipitation. Fig. 6 presents the TEM and EDS results for the N1 (VO₂/TiO₂ (~20 nm)) and N2 (VO₂/TiO₂ (~70 nm)) core/shell particles, respectively. A clear image contrast between the amorphous shell and the crystallised VO₂ core provides estimated coating thicknesses of ~20 nm (Fig. 6-a) and ~70 nm (Fig. 6-c) for samples N1 and N2, respectively. The coatings cover the surface of the rods with a uniform thickness. After annealing, the core/shell interface become obscure (Fig. 6-b and d), which indicates that shell coating has crystallised.

A more detailed microstructural analysis further confirmed that all the coatings crystallised into anatase TiO₂. SAED patterns can distinguish two different materials with good resolving ability. For pure VO₂ single rods, only one set of two-dimensional diffraction rings appeared (Fig. 6-b), whereas another set of SAED patterns with dispersed diffraction rings (red dashed circle) can be well indexed to anatase for core/shell samples N1 (Fig. 6-P1) and N2 (Fig. 6-P2), which is in agreement with the XRD results. The Raman spectra (Fig. 7) of N1 and N2 also indicate that the anatase shell was crystallised; a Raman shift at 143 cm⁻¹ can be attributed to the dominating

Eg(1) vibrational mode in anatase TiO₂³⁶. Other peaks denoted by black figures can be attributed to the vibration modes in VO₂(M1)³⁷. The results from the EDS, Raman and SAED analyses confirm that the coating is primarily composed of anatase. The absence of anatase peaks in the XRD pattern of N1 should primarily be attributed to a relatively small crystal size (Fig. 6-R1, 5~10 nm) and volume fraction.

For N1 with a very thin TiO₂ coating, the surface anatase particles have rather distinguishing morphologies. Some dispersed bright areas appeared on the relatively rough surface of N1 (Fig. 6-b), which should be a result of inhomogeneous expansion and shrinking of the coating during annealing and cooling. High resolution TEM images of the thin edge parts of the coating N1 and N2 are shown in images Fig. 6-R1, R2 and R3. N1 presents an anatase crystal size of ~5 nm (Fig. 6-R1), whereas N2 exhibits a single crystal size of >40 nm (R2) with an incident direction along the zone axis [-121] of anatase, which is confirmed by a set of periodic bright two-dimensional lattice in the SAED image; the interplanar distance exhibited by the lattice fringes is in accordance with that of the (101) plane of anatase. For point R3, the crystals are isolated with a rather small (~a few nanometres) size. Furthermore, the interface between adjacent anatase particles in N1 is very compact (Fig. 6-R1) compared to N2 (Fig. 6-R3).

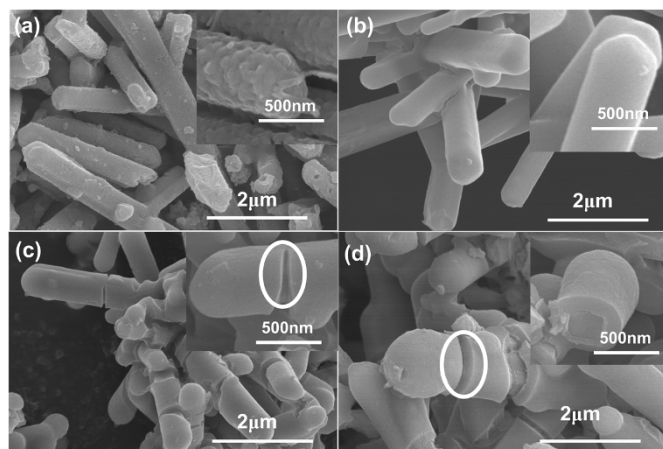


Figure 5 | Morphology of the as-prepared VO₂@TiO₂ core/shell nanoparticles. SEM images of the annealed samples N1(a), N2(b), N3(c), and N4(d) showed clear core/shell structure and thickness-dependent shell morphology. White rings in c and d indicate that the rather thick shell tend to form cracks.

Phase transition. DSC is a very commonly used technique for characterising the first-order phase transition^{12,19,22,23,38} of VO₂ by monitoring the changes in enthalpy. In our work, the transition temperature (T_c, extreme values in heating and cooling cycles) and hysteresis (ΔT, the difference of the T_c in the heating and cooling cycles) for pure VO₂ nanorods are very close to previously reported values (~53.6°C in a cooling cycle and ~64.6°C in a heating cycle, Fig. 8-a)^{12,16,17,35,36}. After annealing (above dashed curves), sample N1 and N2 exhibited an increased T_c in both the heating and cooling cycles, which varied for different samples: 71.6°C (heating)/60.8°C (cooling) for N1 and 70.3°C (heating)/ 62.4°C (cooling) for N2, representing a T_c increase of 6~7°C compared to pure VO₂. In addition, the width of the hysteresis loop (ΔT) of N2 was reduced after annealing from 11°C to 7.9°C, which is not observed for pure VO₂ and is inconspicuous in sample N1. Thirdly, the enthalpy change (for unit mass) during the transition was reduced after coating (Fig. 8-b). This result is expected because TiO₂ does not exhibit a phase transition in this temperature range. Through integration over the peak range, the titania mass content can be quantitatively calculated using the following formula: $W(\text{TiO}_2) = \{1 - I(\text{sample})/I(\text{VO}_2)\} \times 100\%$, where I denotes the integral intensity over the peak range. Based on this calculation (Fig. 8-c),

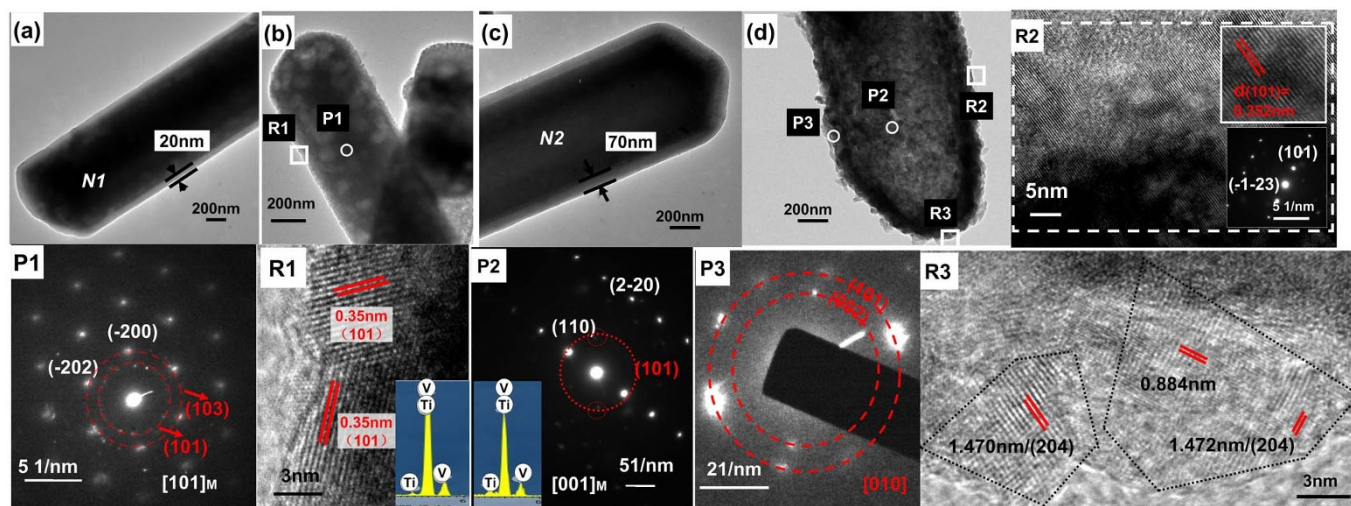


Figure 6 | Microstructure probing of core/shell composite particles by TEM. TEM images for sample N1 and N2. (a) and (b) are images for sample N1 before and after annealing. P1 is SAED pattern for the dot denoted in b, the HRTEM image for dot R1 were shown in Fig. 6R1. (c) and (d) are images for sample N2 before and after annealing. P2 and P3 are the SAED pattern for corresponding dots shown in Fig. 6d. R2,R3 are HRTEM images for two areas in Fig. 6d.

the TiO₂ shell accounts for ~ 29.3 wt% and ~ 51.0 wt% in samples N1 and N2, respectively.

The transition between the semiconducting M1 phase and the metallic R phase generally has a ferroelastic feature^{39,40} that primarily includes two processes: the nucleation of a new phase in the original phase matrix and the boundary diffusion of the hetero-phase (M1&R). The nucleation is thermodynamically activated, which primarily depends on the microstructure (structural or chemical defects, where nucleation always preferentially initiates). The increased T_c indicates that the chemical stability of the M1 phase has increased compared to that of the R phase. Notably, pure VO₂ also exhibits an increase of T_c after annealing (dashed black curves in Fig. 8-a). This result indicates that vacuum annealing can induce internal changes within the VO₂ lattices. Intrinsically, non-stoichiometry³² can result in this change. Excess of oxygen can act as acceptor²¹ and thus increases the stability of monoclinic phase in Al/Cr-doped VO₂ powders²². Recently, Zhang, S³² observed that a deficiency of oxygen (<30 mtorr) stabilised the rutile phase to temperatures as low as 103 K, whereas oxygen-rich growth conditions stabilised the monoclinic phases directly by confocal Raman

nano-probing. Oxygen vacancies are commonly observed in VO₂ polycrystalline films prepared under relatively oxygen-deficient reducing atmospheres. These oxygen defects can exert a considerable influence on the transition temperature⁴¹ because the new phase preferentially nucleates at the defect sites. In our case, the annealing under a relatively oxidative atmosphere (~ 3 torr) most likely increased the T_c.

With the exception of non-stoichiometry, interface effects may inevitably play an important role. Firstly, compositional diffusion at the VO₂-TiO₂ interface was confirmed by compositional scanning TEM analysis of the interfacial distribution of Ti and V elements using an EDS detector, as shown in Fig. 9-a to d. The curves for samples N1 and N2 before (a, b) and after (c, d) annealing exhibited a saddle-like distribution for the titanium content (red curves), with the two saddle points (marked by black sticks) at the interface between core and shell where the thickness of the titania coating reached a maximum. The relative intensity of the K α 1 signals of V and Ti reflected the compositional change before and after annealing. In the gel-coated samples (Fig. 9-a and b), the V intensity with respect to Ti outside of saddle points is very low. In contrast, the V intensity substantially increased after annealing, which implies that some amount of V diffused into the titania lattice. The impact of Ti doping on the dynamic phase transition of VO₂ has been confirmed by previous studies⁴²⁻⁴⁴. V_{1-x}Ti_xO₂ films exhibited lower hysteresis loop widths and increased T_c at higher Ti doping amounts ($\sim 9.4^\circ\text{C}/\text{at.}\%$). A similar interfacial diffusion and Ti-doping can occur at 400°C⁴⁵, 450°C⁴⁶, or 500°C⁴³ for TiO₂/VO₂ multilayer films. Ti-doping forms another metastable M2 phase and induces the formation of internal stress, which is reflected in an increase in the Mott phase transition temperature.

In addition, the interfacial stress caused by the mismatch of thermal expansion/shrinkage between the core and shell materials may be another reason for the modified transition temperature. The average linear expansion coefficient (100 \sim 480°C) is $25 \times 10^{-6} \text{ K}^{-1}$ for VO₂ along c_R and $4.5 \times 10^{-6} \text{ K}^{-1}$ along a_R ⁴⁷, whereas the value for titania is $7.38 \times 10^{-6} \text{ K}^{-1}$ ($a_{||}$) and $3.53 \times 10^{-6} \text{ K}^{-1}$ (a_{\perp})⁴⁸. This mismatch may result in an expansion (or shrinkage) prevailing along the rod length direction (because $c_R[001]$ corresponds to $a_{M1}[100]$), which induces a compressive (when heating) and a tensile (when cooling) stress on the VO₂ rod. For samples N1 and N2 with undamaged coatings, these thermal stresses may not be fully relaxed by microcracks. In our study, structural distortion was confirmed by

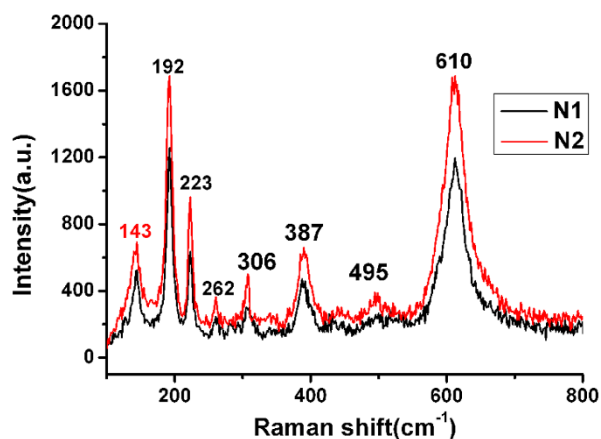


Figure 7 | Compositional and phase identification by Raman spectroscopy. Raman spectra of composite samples N1 (20 nm TiO₂ coating) and N2 (70 nm TiO₂ coating). Peaks denoted by red figures can be indexed to anatase TiO₂, other peaks denoted by black figures can be ascribed to VO₂(M1).

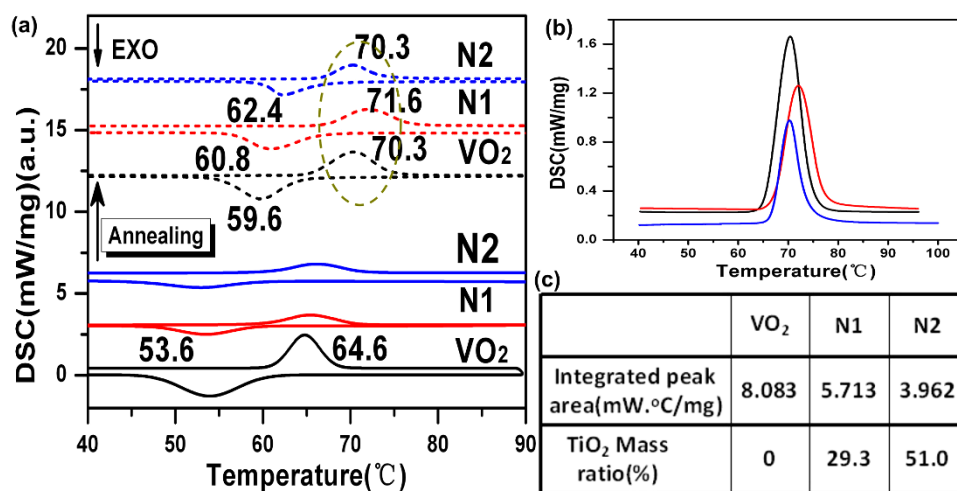


Figure 8 | Phase transition property of the as-prepared VO₂@TiO₂ nanocomposites. (a) DSC curves for: pure VO₂(black curve), sample N1 (red curve) and N2(blue curve) before (below solid curves) and after (above dash curves) annealing. (b) The magnified part of DSC peaks of annealed VO₂, N1 and N2 during heating. Fig. 8c listed the value of integrated area for those three peaks in Fig. 8b and the mass ratio of TiO₂ calculated based on the integral area (refers to the details in the corresponding text).

slow XRD scans of the strongest VO₂(M1) (011) peak (Fig. 10). There are apparent angular peak shifts in the annealed samples (dashed curves) compared to the unannealed ones (solid curves), which indicates that interfacial stress most likely induced the lattice distortion after annealing. The thermal stress changed the defect state and distribution on the local surface, which would have a significant influence on the phase transition behaviour of VO₂. Recently, structural and electronic impacts were observed crossing phase boundaries at high-strain states⁴⁹, whereas oxygen defects could be induced by boundary stress⁵⁰, which jointly affect the phase transition behaviour.

From the above discussion, it appears that the annealing process not only changes the intrinsic stoichiometry of VO₂ but also leads to interfacial diffusion and stress to some degree. Note that although the T_c was increased for our VO₂@TiO₂ particles, the transition temperature can be easily tuned by doping with W¹⁹ and/or Sb¹⁸. In fact,

W-doped VO₂@TiO₂ particles were also synthesised with a W-doping content at ~1.34 at%, and the transition temperature was reduced to 26.5 ~ 35.0°C with 3.5–6.0°C increase as compared to uncoated W-doped VO₂ (see supplementary Figure S5). This temperature range is appropriate for real applications.

Thermochromic property. The assessments of the thermochromic property were only implemented on samples with uniform coatings (samples N1 and N2) to exclude the impact of macrocracks and other uncontrollable irregularities. In our study, the use of Teflon tape as a medium to form the powder coating has particular advantages. Fig. 11-a presents the SEM image of a typical surface of the film, in which the rods are patterned with only one single layer, which is useful for evaluating the properties of the rod with a uniform thickness while eliminating the influence of the dispersing media. Because the size of the nanorods is comparable to the wavelength of the incident radiation, UV-V is diffuse transmittance and reflectance (further denoted as Tr and Re) spectra including the scattering effect were measured, and these results are shown in Fig. 11-b and c (FTIR transmittance and reflectance curves were refers to supplementary Fig. S6). The transmittance hysteresis loop at 2000 nm with various

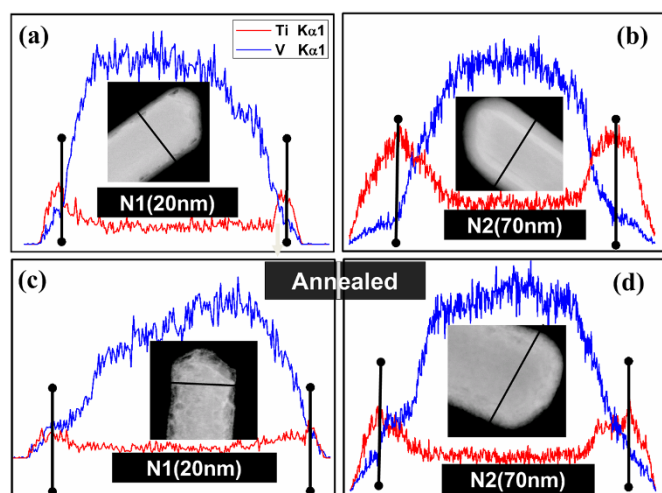


Figure 9 | Confirmation of the interfacial diffusion and Ti-V doping. The compositional scanning TEM curves for: N1 (20 nm titania coating) and N2 (70 nm titania coating) before and after annealing. (a) N1, before annealing; (b) N2, before annealing; (c) N1, after annealing; and (d) N2, after annealing. Insets are dark-field TEM images of the corresponding samples. Scanning were conducted along the black line and signals of Ti and V K α 1 were collected for plotting.

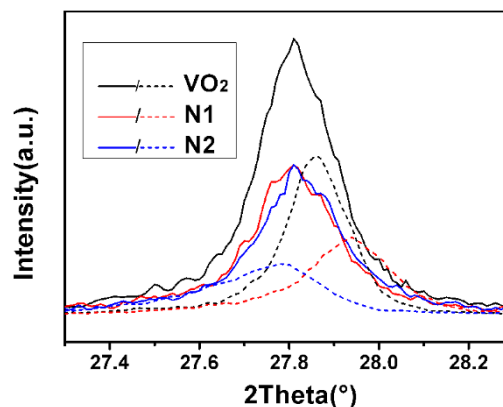


Figure 10 | Confirmation of the structural change after annealing by XRD. The XRD slow scanning curves from 27.3° to 28.3° (peak of (110)_{M1}) for VO₂(black), N1(red) and N2(blue) before (solid curves) and after (dash curves) annealing were shown and clear peak shifts indicated that crystallographic structure was changed after annealing.

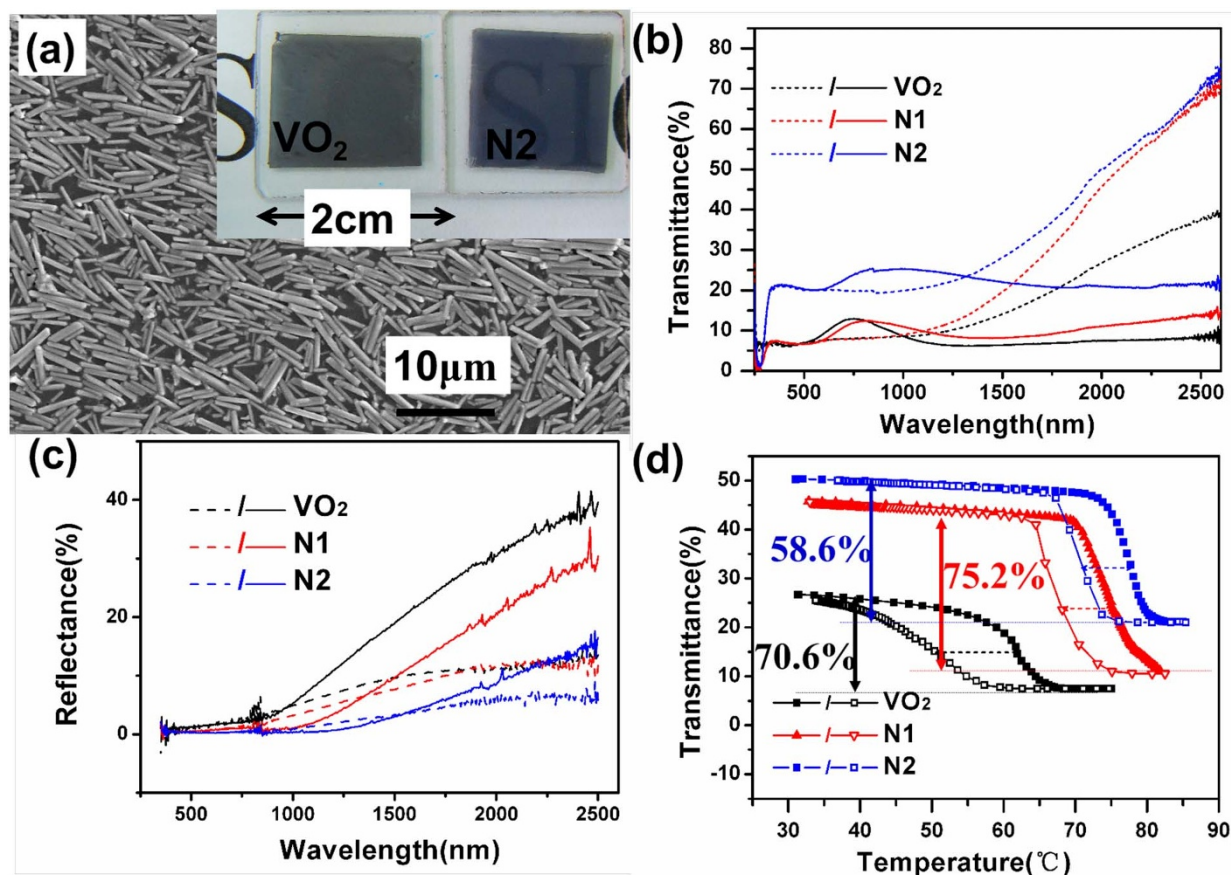


Figure 11 | Thermochromic performance of as-prepared core/shell particles. (a) is the SEM image of one typical film surface. Inset in (a) demonstrates films on glass made of pure VO₂ (left, deep yellow-brown colour) and N2 (right, blue colour, with higher transparency). (b) and (c) are the diffuse transmittance and reflectance spectra in the wavelength range from 250–2500 nm. Samples are: VO₂ (black curves), sample N1 (red curves) and N2 (blue curves) at 25°C (dash curves) and 90°C (solid curves). (d) is the temperature-varied transmittance of those three annealed samples at 2000 nm during heating (solid) and cooling (hollow) cycles.

temperatures is shown in Fig. 11-d. Both N1 and N2 exhibited conspicuous infrared modulability, and the transmittance modulation ability and luminous transmittance are summarised in Table 2.

Neither Teflon tape nor TiO₂ have thermochromic properties; therefore, the change in the Tr and Re with temperature should be due to the phase transition of the VO₂ particles. The entire spectral range in question can be divided into two regions: at a shorter wavelength region A the transmittance at 90°C is higher than 25°C; and at a longer wavelength region B the transmittance at 25°C is much higher than that at 90°C (the so-called IR switching). In the region B, the Tr behaviour is very conventional for VO₂, in which the Tr is lower at temperatures above the T_c (metallic R phase) than that at lower temperatures (semiconducting M1 phase). The plasma frequency (ω_p) for the R phase in polycrystalline thin films is reported to be 1.0 eV ($\sim 1.24 \mu\text{m}$)⁵¹ or 1.6 eV ($\sim 775 \text{ nm}$)⁵², which is proportional to the free-electron concentration and depends on the temperature and the film/substrate interface state. Hence, the metallic R phase has a lower transmittance and higher reflectance in the IR region ($\omega < \omega_p$). However, semiconducting VO₂(M1) has a band gap at approximately 0.7 eV; therefore, it is highly transparent to photons with energies less than E_g ($\lambda > \sim 1.77 \mu\text{m}$). However, at the region A including the whole visible part, the R phase exhibited a higher transmittance than low-temperature M1 phase, although both transmittances were at a relatively low level (<30%) because of intrinsic absorption. This reverse transmittance cause undesirable minus modulation for solar energy as shown in Table 2. This behaviour deteriorate the whole efficiency and may be a considerable drawback for applications that require

good visual senses; whereas, such a coating can be used for energy-saving wall paint/coatings or the rear windows of cars. As illustrated in Fig. 11-a, there are interspaces among rods, typically several tens of nanometres to submicrons. Therefore, the transmittance of our as-prepared samples in region A should primarily be attributed to light transmittance from the uncovered areas of the Teflon tape and the light scattered by the VO₂ rods in the forward direction. Mie scattering predominates because the rod thickness (500–600 nm) was very similar to the wavelength of the incident visible light. According to Mie theory⁵³, scattering rises to a maximum when it is the same as the characteristic length of the scattering centre (the rod thickness), and then it decays to zero towards longer wavelengths. Therefore, the Tr change before and after the Mott transition in this region should contribute to the different scattering abilities of the VO₂ composite particles. The M1 phase scatters light more strongly due to its larger refractive index ($n(\text{VO}_2(\text{M1})) = 2.7 \sim 2.8$, $n(\text{VO}_2(\text{R})) = 2.0 \sim 2.5$)^{15,54}, which can lead to smaller transmittance than that of the R phase. In particular, after being coated with highly-transparent TiO₂, the composite films exhibited considerably improved luminous transparency. As shown in Fig. 11-a, the 70 nm TiO₂ coating (N2) significantly increased the luminous transmittance, from $\sim 8\%$ to $\sim 27\%$ (Table 2). The transparent TiO₂ coating accounts for a considerable part of the total film in thick N2 samples, which increases the total visible transmittance.

For a pure VO₂ film, the modulation ability at 2 μm is $\sim 70.6\%$ with a large hysteresis loop width (more than 10°C). The TiO₂-coated composites exhibited a modified optical switching property,



Table 2 | Summary of solar and luminous transmittance

VO ₂	Normalized solar transmittance (T _{sol})				Luminous transmittance (T _{lum})	
	Region A: 250~1000 nm (73.7%)		Region B: 1000~2500 nm (26.3%)		(380~780 nm)	
	25°C	90°C	25°C	90°C	25°C	90°C
	7.52%	9.55%	14.01%	7.07%	7.35	8.21
	ΔT _{sol}		ΔT _{sol}		ΔT _{sol}	
	-2.03%		6.93%		6.93%	
N1	Region A: 250~1100 nm (80.6%)				Region B: 1100~2500 nm (19.4%)	
	25°C	90°C	25°C	90°C	25°C	90°C
	7.67%	9.26%	23.61%	9.27%	11.55	11.80
	ΔT _{sol}		ΔT _{sol}		ΔT _{sol}	
	-1.58%		14.34%		11.55	
N2	Region A: 250~1315 nm (89.0%)				Region B: 1315~2500 nm (11.0%)	
	25°C	90°C	25°C	90°C	25°C	90°C
	20.22%	22.5%	39.02%	21.39%	27.46	27.41
	ΔT _{sol}		ΔT _{sol}		ΔT _{sol}	
	-2.28%		17.63%		17.63%	

^aConsidering that the IR switching ranges for as-prepared samples are different, the total solar spectrum range was separated into two parts: region A with shorter wavelength where the transmittance in 90°C is higher than 25°C, and region B with longer wavelength where the transmittance in 25°C is much higher than that in 90°C (the so-called IR switching). 1000–2500 nm for pure VO₂, 1100–2500 nm for N1 and 1315 nm–2500 nm for N2 were used for switching efficiency calculation in the range B. The solar transmittance in the specified range is calculated by such formula: $T_{sol} = \int \phi(\lambda) \cdot Tr(\lambda) \cdot d\lambda / \int \phi(\lambda) \cdot d\lambda$, in which $\phi(\lambda)$ is the solar irradiance spectrum for air mass 1.5 corresponding to the sun standing 37° above the horizon and $Tr(\lambda)$ is the transmittance of our sample⁶. The solar transmittance modulation efficiency was calculated by $\Delta T_{sol} = T_{sol,90^\circ C} - T_{sol,25^\circ C}$.

^bLuminous transmittance (T_{lum}) is calculated by such formula: $T_{lum} = \int \phi_{lum}(\lambda) \cdot Tr(\lambda) \cdot d\lambda / \int \phi_{lum}(\lambda) \cdot d\lambda$, in which $\phi_{lum}(\lambda)$ is the relative sensitivity of human eye on visible light. Integral was taken from 380 nm to 780 nm, details can be found in our recent work⁷.

both in the modulation level and hysteresis loop width (Fig. 11-b and d). A 70 nm TiO₂ coating (sample N2) exhibits a largely increased transmittance in both the M1 and R states, but with somewhat deteriorated modulation ability (~58.6%). A thinner 20 nm coating (sample N1) can also increase the transmittance by a small degree with maintained modulability (~75.2%). Furthermore, the TiO₂ coating can significantly decrease the transition hysteresis, which is in agreement with the DSC measurements. However, films prepared using powders in previous studies commonly exhibited a very wide hysteresis. We prepared films based on VO₂ nanoparticles with large hysteresis (~21°C) and VO₂@SiO₂ composite particles with very wide transition range (~30°C). Lu, Z⁵⁵ prepared a VO₂/PEGDA film with hysteresis at ~25°C. Our composite particles with considerably reduced hysteresis will benefit future applications for rapidly responding and high-precision controlled materials. The diffusion of Ti into VO₂ will weaken its IR switching property due to the introduction of lattice defects⁴⁵. N2 with considerable Ti-V diffusion will clearly exhibit reduced modulability. However, the significantly enhanced transmittance and reduced hysteresis may compensate for this weakness, and further investigations on optimising the VO₂ size and coating thickness will be required to achieve better integrated performance.

As previously mentioned, VO₂ films have an intrinsic yellow-brown colour and the pure VO₂ film exhibits a dark colour, as shown in Fig. 11-a, inset (left). However, N2 with a 70 nm TiO₂ coating exhibits a more transparent blue colour (Fig. 11-a, inset (right)). This result implies that the 70 nm titania coating modified the colour of the film. Calculations of the optical interference effect in the sandwiched 70 nmTiO₂/500 nmVO₂/70 nmTiO₂ ($n_{air} < n_{TiO_2} < n_{VO_2}$ ¹⁶) structure suggest that the 70 nm TiO₂ coating can serve as an effective anti-reflecting coating for red light ($\lambda \sim 700$ nm, $\lambda = 4 \times n \times d$, n is the average refractive index of anatase, $n \approx 2.5$, and d is the thickness of the TiO₂ coating, $d \approx 70$ nm). Furthermore, the incidental short wavelength light (~300–400 nm) is reduced by a large degree because of the existence of UV-absorbing TiO₂. Therefore, the TiO₂ coating changed the spatial distribution of the scattered visible light, by which we can observe the reflected blue colour. This coating effectively changed the appearance of the film. In summary, TiO₂ coatings can effectively increase the luminous transmittance and modify the colour of films. The modified blue colour is considerably more favourable and acceptable as a functional and decorative coating.

For practical application, W-doped composites with lower transition temperature were also considered. The UV-Vis spectra were shown in Fig. 12. The transmittance curves and hysteresis loops showed a similar law as undoped VO₂: after coating, the average transmittance was increased with deteriorated modulation ability; the loop width was also narrowed down by 5.7°C. Meanwhile, the coated sample showed a light blue colour in comparison with yellow one of uncoated VO₂:W film. As compared with undoped films, the IR switching efficiency is diminished because of the incorporation of W dopant, as reported elsewhere. However, the core/shell particles show a modified colour of light blue, which is more comfortable for human sense.

For energy-efficient smart window, the as-prepared particles are so large that scattering and absorption dominate the solar modulation, which results in a very small efficiency and may inappropriate for practical application by now. However, VO₂ particles with much smaller size (short diameter < 50 nm) was synthesized according to the literature²³. VO₂@TiO₂ nanoparticles with shell thickness 1~7 nm has been successfully prepared and showed an excellent solar efficiency of 10.27% (Fig. 13). However, as shown in Fig. 13-c and f, no colour modification or obvious interfacial effect on transition was observed by now. The effect of interfacial Ti-V doping and stress on the phase transition temperature were inconspicuous because of relatively thin coating.

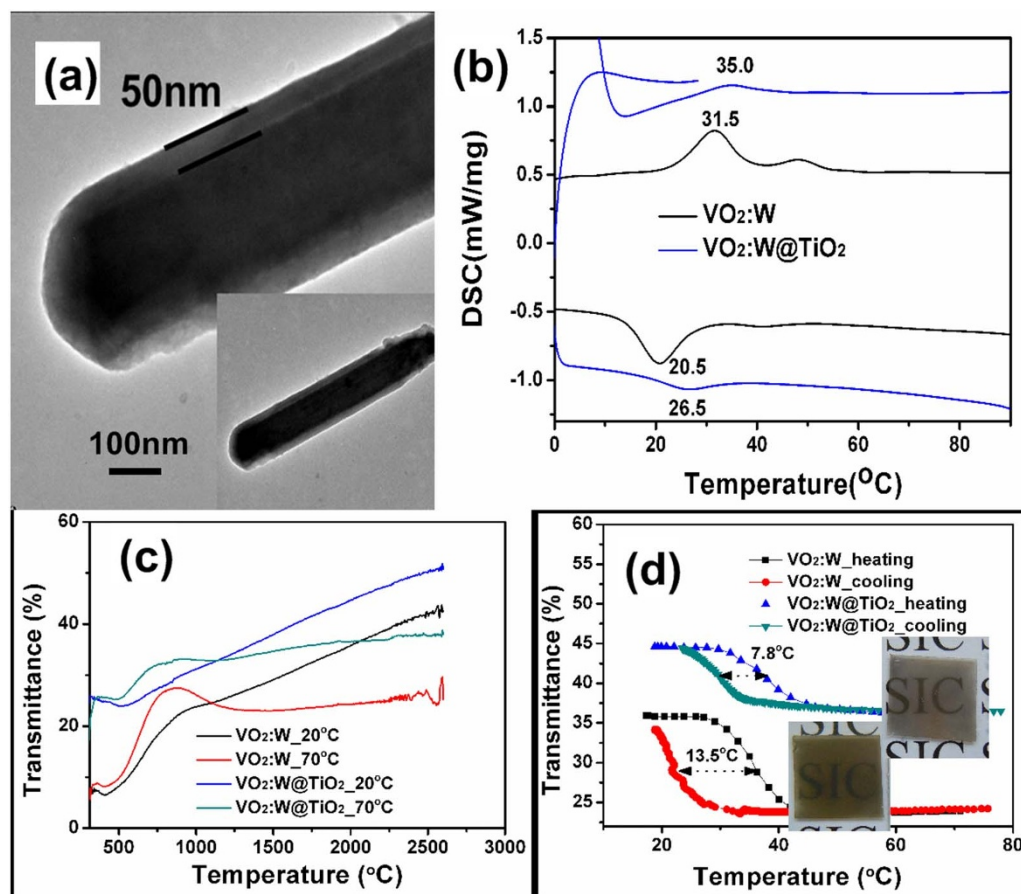


Figure 12 | $\text{VO}_2\text{:W@TiO}_2$ nanocomposites with a solar modulation ability at room temperature. By the sol-gel coating method, we successfully prepared $\text{VO}_2\text{:W@TiO}_2$ powders (a). The DSC curves are shown in Fig. 12b. After W-doping, the transition temperature has been reduced to 20~30°C and after coating the transition temperature was increased by 3.5°C (heating cycle) and 6°C (cooling cycle). The films of the $\text{VO}_2\text{:W}$ and $\text{VO}_2\text{:W@TiO}_2$ powders were prepared in the same method described in “Methods” section with the same solid loading content. The transmittance curves and hysteresis loops showed a similar law (Fig. 12c and d): after coating, the average transmittance was enhanced whereas with deteriorated modulation ability; the loop width was also narrowed down by 5.7°C with increased transition temperatures both in heating and cooling cycles. Meanwhile, the coated sample showed a modified light blue colour in comparison with the yellowish one of uncoated $\text{VO}_2\text{:W}$ film.

Photocatalytic properties. The photocatalytic properties of our samples were investigated by monitoring the decomposition of Rhodamine B (RhB) under simulated solar light produced by irradiation from a Xe-lamp (240 nm~2 μm). For comparison, 0.128 g of the N1 and 0.073 g of the N2 composite powders were used in each experiment to maintain a constant titania content (according to the titania mass ratio calculated from the previous DSC results). In addition, 0.1 g of VO_2 was applied to determine whether VO_2 itself has photocatalytic properties. Before light irradiation, the adsorption behaviours of RhB over the three samples were examined under dark conditions. The adsorption-desorption equilibriums could be established within 1 hour for all the samples. The amounts of RhB adsorbed on the surfaces of the samples are listed in Table 3. The TiO_2 coated samples exhibited enhanced adsorption abilities. On the basis of the same initial RhB concentration, as high as 60%, 81% of RhB was adsorbed onto the catalyst surface over the N1 and N2 samples compared to only 22% over the uncoated VO_2 sample. The enhanced adsorption abilities for RhB with respect to the pure VO_2 can be attributed to the significantly increased surface areas of samples (Table 3) and particularly to the considerably stronger adsorption ability of porous titania.

The temporal UV-Vis spectral evolution of the RhB aqueous solution for these three samples during the photocatalytic degradation reactions are plotted in Fig. 14. Pure VO_2 has negligible

photocatalytic degradation ability for RhB (after excluding the impact of the natural degradation of RhB and adsorption under the same illumination conditions), whereas the coated samples N1 and N2 can both degrade the RhB dyes with a considerable efficiency at a given time (67.4%~69.6% for 2.5 h). The primary absorbance that maximised at ~554 nm markedly decreased with irradiation time. Comparison experiments demonstrated that the photolysis of RhB without a catalyst was very slow (brown curve) and that RhB could not be degraded in the presence of samples under dark conditions, which implies that the degradation of RhB in the present study is indeed through a photocatalytic process.

Furthermore, both of these composite samples have higher specific surface area values than the theoretical values obtained through a simple calculation based on an ideal close-packed coating (refers to supplementary Fig. S7), which indicates that the crystals of the sample surfaces are far from closely-packed. This result is in agreement with the microstructures observed previously, where the interface between adjacent anatase particles in N1 is relatively compact (Fig. 6-R1) compared to N2 (Fig. 6-R3). A certain amount of micro-/nanopores or cracks composed the majority of the total surface area, especially in sample N2. A larger specific area can ensure more active sites for adsorption and subsequent reactions, but desorption of the degraded species will be significantly hindered if they reside in the inner space, which will in turn reduce the entire degradation efficiency. This may be the reason why sample N2,

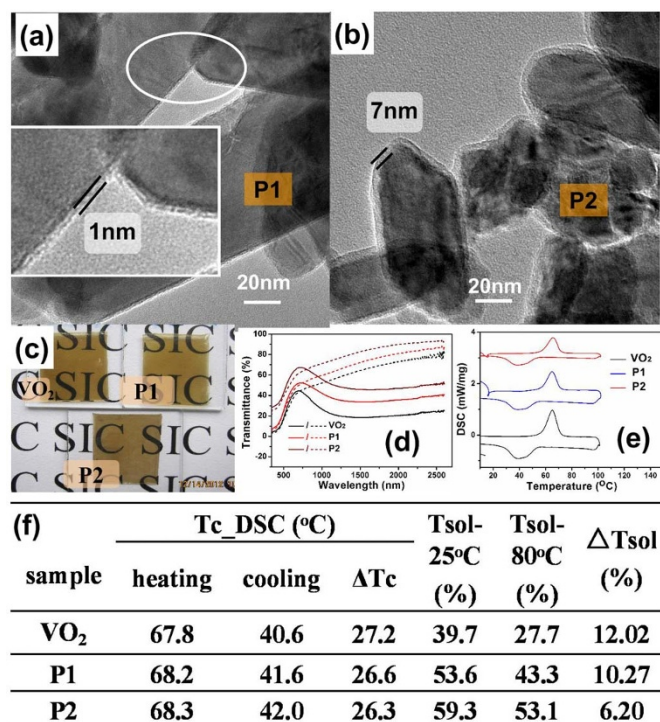


Figure 13 | VO₂@TiO₂ nanoparticles with excellent solar modulation efficiency. VO₂@TiO₂ nanoparticles with short diameter ~50 nm were prepared by ultrasonic-assisted hydrolysis. The shell thicknesses of sample P1 and P2 can be estimated from (a) and (b) to be 1 nm and 7 nm, respectively. The photograph of the films and the corresponding transmittance spectrum were shown as below in Fig. 13c and d, respectively, the solid and dash curves are corresponding to the spectra collected at 90°C and 25°C. However, no obvious colour change was found in this system. P1 and P2 with size ~<50 nm will exhibit relatively small scattering and absorption for visible light in comparison with the big composite particles N1 and N2. As shown in Fig. 13f, as high as 10.27% of solar modulation efficiency can be obtained by the film of P1 powders. However, P1 and P2 didn't exhibit much variation in the transition temperatures and hysteresis (Fig. 13e).

which had a considerably larger specific surface area than sample N1, did not exhibit considerably enhanced degradation ability. In addition to the specific surface area, other factors such as surface defects, carrier concentrations and carrier transfer rate will also affect the final photocatalytic performance. Modifications of the microstructure can effectively adjust the photocatalytic performance. Compared to other core/TiO₂ particles^{56,57}, the photocatalytic efficiencies of the as-synthesised samples are not very satisfactory, which is most

Table 3 | Adsorption ability and Specific surface area of pure VO₂, N1 (VO₂@20 nmTiO₂), and N2 (VO₂@70 nmTiO₂) based on N₂ adsorption measurements (A_{me}), or calculation with ideal closely-packed surface postulate (A_{cal})

Sample number	RhB adsorption (%)	Specific Area A _{me} (m ² /g)	Specific Area A _{cal} ^a (m ² /g)
VO ₂	22	1.66	1.72
N1	60	4.97	1.84
N2	81	33.40	2.11

^aCalculation were conducted under assumption that coatings were composed of compactly-packed TiO₂ particles (Suppose the titania coating/shell is composed of compactly-packed nanoparticles, and there is no macropores, the specific surface area are dominantly composed of the outer surface of titania. refers to S7).

likely due to their uncompetitive surface areas. On-going research on VO₂@TiO₂ nanocomposite particles with smaller core size may provide more exciting performance, which will be reported in the near future.

To exclude the heating effect from the high power irradiation, we placed the sample into an ice water bath during the reaction. We note that VO₂ remains chemically stable after 2 hours of light exposure. The XRD patterns of the irradiated N1 and N2 samples are shown in S8.

Enhanced chemical stability against oxidation. To explore whether the titania coating will improve the oxidation resistance of the as-prepared VO₂@TiO₂ composite particles, annealing in air at different temperatures for the same amount of time (15 min) was conducted with a heating rate of 10°C/min on three samples. The phase evolution after annealing is shown in Fig. 15-a. VO₂ will readily oxidise into V₃O₇ or V₂O₅ at temperatures greater than 290°C. In contrast, the coated N1 and N2 samples remained chemically stable until 320°C, which suggests that the titania shell can act as an effective barrier layer for the diffusion of oxygen into the VO₂ lattice.

Thermogravimetric analysis (TGA, Netzsch STA449C, under air) provided a more subtle perspective for monitoring the complete oxidation process. Fig. 15-b presents the results from the TGA of three samples (pure VO₂ (black curve), VO₂@TiO₂ (20 nm) (red curve), and VO₂@TiO₂ (70 nm) (blue curve)). The sample mass began to increase at certain temperature values (shown by arrows), which indicate the onset of oxidation. Compared to ~301°C for pure VO₂, the characteristic temperature for the TiO₂-coated N1 and N2 samples increased to ~336°C and 343°C, respectively. Furthermore, the anatase-coated samples exhibited no clear mass losses, which indicate that the titania species were almost crystallised and that residual organic species scarcely exist. The crystallised TiO₂ shell can enhance the oxidative resistance of VO₂, which is of significant importance for practical applications.

Discussion

Our results demonstrate a new approach to control the optical and Mott transition properties by modifying the surface/interface state and microstructure of VO₂ particles with core/shell nanotechnology. TiO₂ coating can not only enhance the chemical stability of VO₂ but also exhibits the potential to control the transition temperature and hysteresis by designed "interfacial doping" with Ti through annealing. Such "interfacial doping" has the advantage of avoiding the introduction of a large amount of defects as compared with bulk doping. Bulk defect will deteriorate the modulation ability of VO₂ to a large degree. We expect that other cationic or anionic ions for example, Mo, W, Cr, F etc, which can adjust the transition property by bulk doping may also be designed to achieve "interfacial doping" through core/shell nanotechnology, thus to modify the phase transition of VO₂ without bringing in excessive defects and retain a comparably sound switching efficiency as in pure VO₂.

By changing the thickness of TiO₂ shell, the distribution of scattered and transmitted light can be tuned to satisfy an anti-reflecting effect on a micro single-particulate scale (300~600 nm). We can expect such a colour modification can be only realized in particles with size comparable to visible light where scattering plays an important role in the light-matter interactions. The colour of smaller VO₂ particles (~<50 nm) cannot be effectively changed by TiO₂ coating, as shown in Figure 13.

The photocatalytic property of anatase TiO₂ coating can be affected by grain size, deflection, and boundary states. We expect a better photocatalytic property can be obtained by adjusting the annealing program. This integrated structure combining solar-light driven environmental purification with energy modulation can make better use of the solar energy. We foresee the potential of nanocomposite of

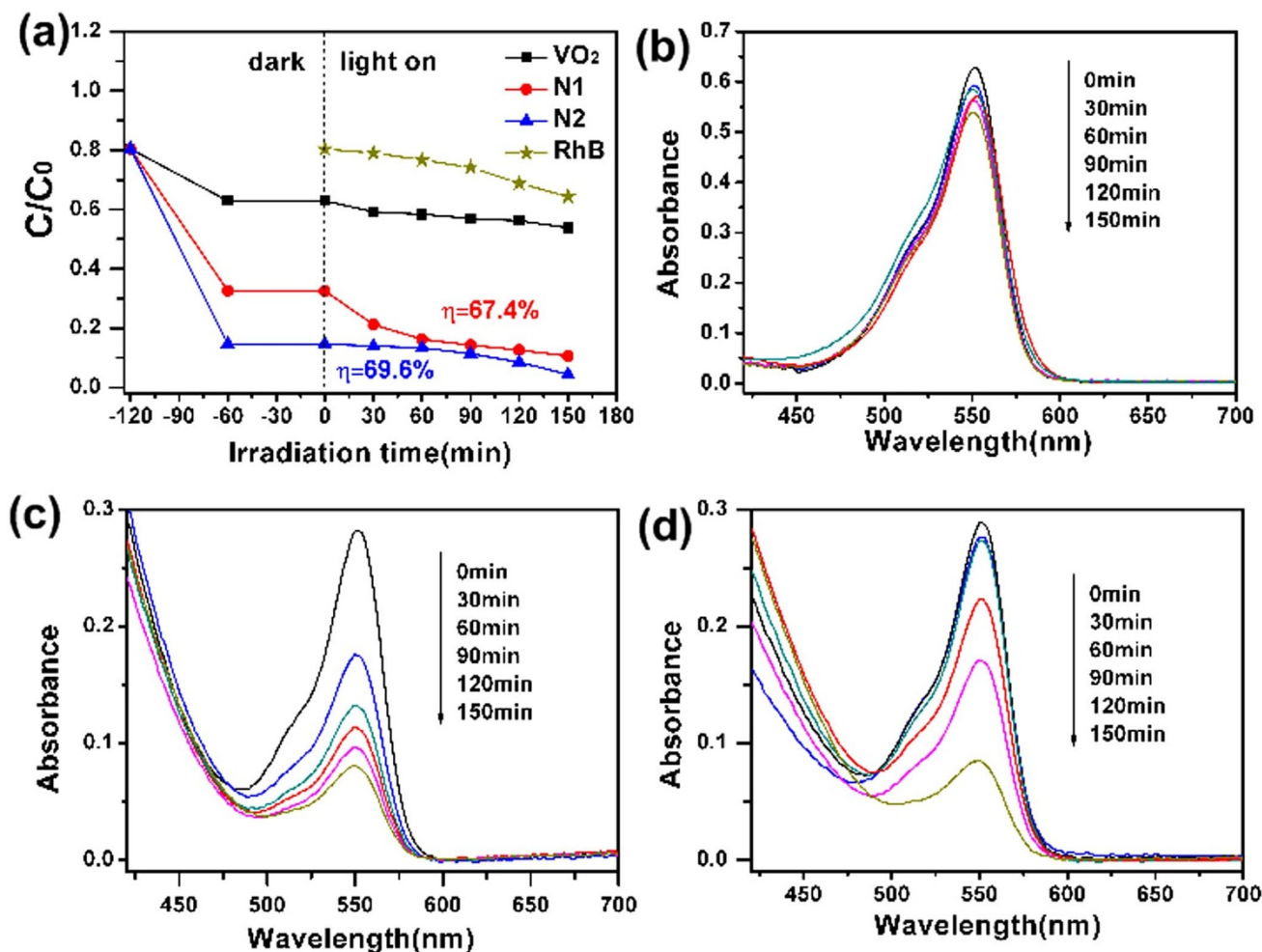


Figure 14 | Evaluation of photocatalytic property. (a) The RhB concentration change with varied reaction time, for adding VO₂ (black curve) and VO₂/TiO₂ composites N1 (red curve) and N2 (blue curve) samples, yellow curve is the natural degradation curve of RhB under the same illumination condition. (b), (c), and (d) are the UV-Vis spectra evolution of RhB aqueous solution in corresponding systems: pure VO₂ (b), N1 (c), N2 (d).

VO₂ with other functional materials, such as light harvesting/conversion materials, to get combined or mutually optimized multi-functions for solar energy conversion or modulation.

Methods

Preparation of VO₂ nanorods. Single-crystal VO₂ nanorods were prepared following a previous work by our group¹⁸. V₂O₅ (Sinopharm Chemical Reagent Co.Ltd, China) and oxalic acid powders (H₂C₂O₄·2H₂O, Wako, Japan) were directly added in a 1:2 molar ratio to 200 mL of deionised water ([V] = 0.037 M) at room temperature. The suspension was continuously stirred until a clear dark blue solution was formed. Then, 40 mL of the suspension was transferred into a 100 mL Teflon-lined autoclave after adjusting its pH to ~1.85 by adding a H₂SO₄ (0.5 M) aqueous solution. After the hydrothermal treatment at 260 °C for 48 h, the autoclave was naturally cooled to room temperature. The resulting black-coloured precipitate was collected by filtration, washed alternatively 3 times with deionised water and alcohol, and then dried at 60 °C in air for 10 h.

Preparation of VO₂@TiO₂ core/shell nanorods. To prepare the VO₂@TiO₂ core/shell nanostructures, 0.03~0.25 g of the as-synthesised VO₂ nanorod powders was ultrasonically dispersed in 80 mL of water-free ethanol (Sinopharm Chemical Reagent Co.Ltd, China) to obtain a well-dispersed suspension. Then, 500 μL~1 mL of titanium tetrabutoxide (TBOT, Sigma Aldrich, reagent grade, 97%) was rapidly added into the suspension under vigorous stirring in an ice water bath for 20 min. The suspension was then transferred into a three-neck flask that was immersed in a constant-temperature water bath at 80 °C. Subsequently, the controlled hydrolysis of TBOT was initiated by adding ~20 mL deionised water/ethanol mixture (50 mL/L) dropwisely. As have shown in the results part, the thickness of the shell can be easily tuned by varying the experimental parameters, which primarily include the loading amount of VO₂, the volume of TBOT and the concentration of H₂O. The as-prepared core-shell powders were collected by filtration, washed twice with ethanol, and then dried in a vacuum oven at 60 °C for 6 h.

To obtain a crystalline coating, the as-synthesised powders were placed into an alumina crucible and then annealed in a vacuum quartz-tube furnace under a flow of air at specific air pressure and temperature. To avoid VO₂ oxidation, the annealing process was optimised. Typically, with an air pressure of ~3 torr, the sample was heated from ambient temperature to 400 °C at a heating rate of ~10 °C/min, and then held at 400 °C for 15 min before naturally cooling to room temperature.

Characterisation. X-ray diffraction (XRD) analyses were conducted on a Rigaku Ultima IV diffractometer with Cu K α radiation ($\lambda = 1.5418 \text{ \AA}$) using a voltage and current of 40 kV and 40 mA, respectively. Unless stated otherwise, all the samples were measured at a scanning rate of 3°/min. The microscopic morphology was obtained using a field-emission scanning electron microscope (FE-SEM, HITACHI S-3400, Japan) at an acceleration voltage of 15 kV. The microstructure and composition of the samples were further analysed using a transmission electron microscope (TEM, JEOL2010) with an energy-dispersive spectrometer (EDS) attachment. Scanning TEM was operated in dark field imaging mode. The Raman spectra of the composite samples were measured using a Raman microscope (Renishaw in Via) with a 514 nm laser source at an input power of 1 mW. This small power was applied to avoid local heating effects. The phase transition behaviours of the resulting products were measured by differential scanning calorimetry (DSC200F3, NETZSCH) over the temperature range from 0 to 90 °C using a liquid nitrogen cooling unit. The heating and cooling rates were set at 10 °C/min.

Photocatalytic reaction. ~0.1 g of the powder samples were ultrasonically dispersed in 50 mL deionized water followed by the addition of 500 μL of a 0.01 M rhodamine B (RhB) aqueous solution. The mixture was then stirred under darkness for 2 h to achieve adsorption-desorption equilibrium. Subsequently, the suspension with continuous stirring was exposed under a Xe lamp (300 W) with an incident direction normal to the surface of the solution. At given irradiation intervals, ~3 mL aliquots of the suspension were collected and separated by centrifugation. The absorption spectrum of the supernatant was measured using a UV-Vis spectrometer (HITACHI U-3010). The concentration of RhB was determined by monitoring the changes in the

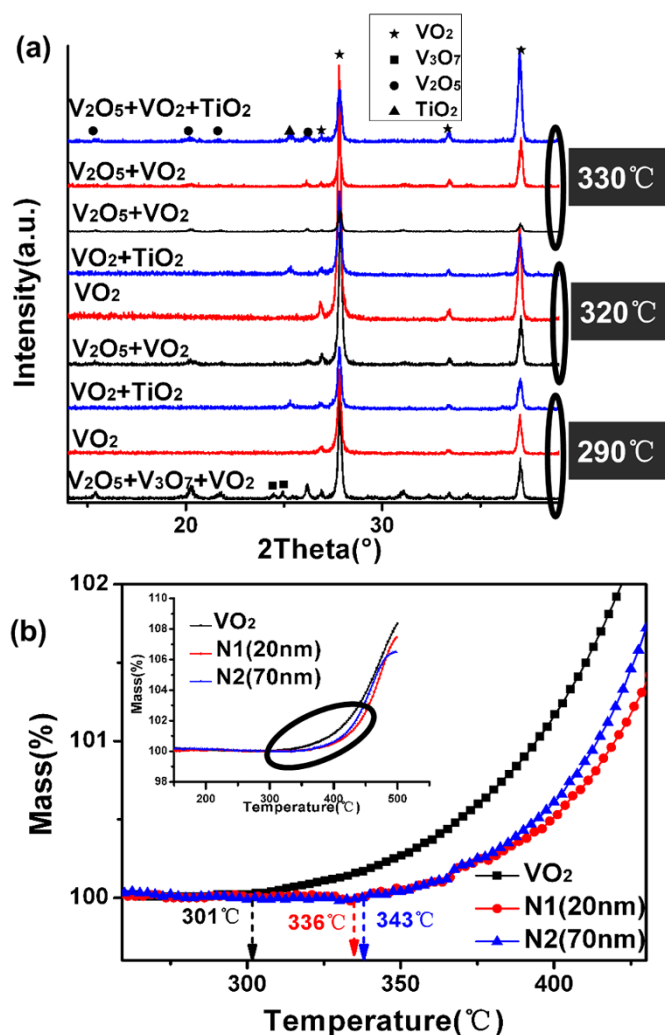


Figure 15 | Enhanced oxidation-resistant ability after TiO₂ coating. (a) plots the XRD results of phase evolution for pure VO₂ (black curve), N1 (red curve) and N2 (blue curve) after annealing at different temperatures in the air. (b) shows TG curves for pure VO₂ (black curve), N1 (red curve) and N2 (blue curve) sample powders.

absorbance maximum at ~ 554 nm. According to the Lambert-Beer law, the absorbance is proportional to the concentration of a dilute solution. The specific surface area was measured on an ASAP2010 (Micromeritics, U.S.A) instrument using the N₂ adsorption method with BET analysis.

Evaluation of the thermochromic properties. Films made of the obtained samples were prepared by coating the powder onto a float glass substrate. For measuring, a piece of double-sided thermal-resistant teflon tape was stuck onto a glass substrate. A stock suspension with solid loading amount of 3wt% was prepared by dispersing a certain amount of powder ultrasonically in ethanol. Then a film was made by casting the suspension solution by anilox roll on the Teflon-tape. After natural drying, repeating this process for twice or 3 times to make sure the whole surface was coated by powders, and then compressed air gun was used to blow away redundant powders which weren't stuck on the teflon surface. The diffuse transmittance (Tr) and reflectance (Re) measurements of the film at the wavelength range from 250 nm to 2600 nm at 25°C and 90°C were conducted using a UV-Vis spectrophotometer (HITACHI U-3010) with an integrating sphere and a temperature controlling unit. The transmittance curve of the sole tape-sticked glass is calibrated as baseline for transmittance measurements.

1. WBCSD, Switzerland Energy efficiency in buildings-Business realities and opportunities(summary report). *World Business Council for Sustainable Development WBCSD, Switzerland* <http://www.wbcd.org/home.aspx> (2009).
2. Granqvist, C. G. Transparent conductors as solar energy materials: A panoramic review. *Solar Energy Materials and Solar Cells* **91**, 1529–1598 (2007).
3. Morin, F. J. Oxides which show a metal-to insulator transition at the neel temperature. *Phys.Rev.Lett.* **3**, 34–36 (1959).

4. Andersson, G. Studies on Vanadium oxides. I. Phase analysis. *Acta Chem.Scand* **8**, 1599–1606 (1954).
5. Jin, P. & Tanemura, S. Formation and Thermochromism of Vo(2) Films Deposited by Rf Magnetron Sputtering at Low Substrate-Temperature. *Jpn J Appl Phys* **1** **33**, 1478–1483 (1994).
6. Qureshi, U., Manning, T. D., Blackman, C. & Parkin, I. P. Composite thermochromic thin films: (TiO₂)-(VO₂) prepared from titanium isopropoxide,VOCl₃ and water. *Polyhedron* **25**, 334–338 (2006).
7. Kang, L. T. *et al.* Effects of Annealing Parameters on Optical Properties of Thermochromic VO₂ Films Prepared in Aqueous Solution. *J. Phys. Chem. C* **114**, 1901–1911 (2010).
8. Zhang, Z. *et al.* Solution-based fabrication of vanadium dioxide on F:SnO₂ substrates with largely enhanced thermochromism and low-emissivity for energy-saving applications. *Energy & Environmental Science* **10**, 4290–4297 (2011).
9. Zhang, Z. *et al.* Thermochromic VO₂ Thin Films: Solution-Based Processing, Improved Optical Properties, and Lowered Phase Transformation Temperature. *Langmuir* **26**, 10738–10744 (2010).
10. Gao, Y. *et al.* Nanoceramic VO₂ thermochromic smart glass: A review on progress in solution processing. *Nano Energy* **1**, 221–246 (2012).
11. Gao, Y. *et al.* Enhanced chemical stability of VO₂ nanoparticles by the formation of SiO₂/VO₂ core/shell structures and the application to transparent and flexible VO₂-based composite foils with excellent thermochromic properties for solar heat control. *Energy & Environmental Science* **5**, 6104–6110 (2012).
12. Ji, S. D., Zhao, Y., Zhang, F. & Jin, P. Direct formation of single crystal VO₂(R) nanorods by one-step hydrothermal treatment. *Journal of Crystal Growth* **312**, 282–286 (2010).
13. Gao, Y. *et al.* Phase and shape controlled VO₂ nanostructures by antimony doping. *Energy & Environmental Science* **5**, 8708–8715 (2012).
14. Ohno, T., Sarukawa, K., Tokieda, K. & Matsumura, M. Morphology of a TiO₂ Photocatalyst (Degussa, P-25) Consisting of Anatase and Rutile Crystalline Phases. *Journal of Catalysis* **203**, 82–86 (2001).
15. Jin, P., Xu, G., Tazawa, M. & Yoshimura, K. A VO₂-based multifunctional window with highly improved luminous transmittance. *Jpn J Appl Phys* **2** **41**, L278–L280 (2002).
16. Mlyuka, N. R., Niklasson, G. A. & Granqvist, C. G. Thermochromic multilayer films of VO₂ and TiO₂ with enhanced transmittance. *Solar Energy Materials and Solar Cells* **93**, 1685–1687 (2009).
17. Evans, P., Pemble, M. E., Sheel, D. W. & Yates, H. M. Multi-functional self-cleaning thermochromic films by atmospheric pressure chemical vapour deposition. *J Photoch Photobio A* **189**, 387–397 (2007).
18. Gao, Y. F. & Wang, Z. Phase and shape controlled VO₂ nanostructures by antimony doping. *Energy & Environmental Science* **9**, 8708–8715 (2012).
19. Cao, C. X., Gao, Y. F. & Luo, H. J. Pure Single-Crystal Rutile Vanadium Dioxide Powders: Synthesis, Mechanism and Phase-Transformation Property. *Journal of Physical Chemistry C* **112**, 18810–18814 (2008).
20. Nag, J. & Haglund, R. F. Synthesis of vanadium dioxide thin films and nanoparticles. *Journal of Physics-Condensed Matter* **20**, 1–14 (2008).
21. Whittaker, L., Jaye, C., Fu, Z. G., Fischer, D. A. & Banerjee, S. Depressed Phase Transition in Solution-Grown VO₂ Nanostructures. *Journal of the American Chemical Society* **131**, 8884–8894 (2009).
22. Wu, C. *et al.* Direct hydrothermal synthesis of monoclinic VO₂(M) single-domain nanorods on large scale displaying magnetocaloric effect. *Journal of Materials Chemistry* **21**, 4509–4517 (2011).
23. Ji, S., Zhang, F. & Jin, P. Preparation of high performance pure single phase VO₂ nanopowder by hydrothermally reducing the V₂O₅ gel. *Solar Energy Materials & Solar Cells* **95**, 3520–3526 (2011).
24. Parker, J. C. Raman scattering from VO₂ single crystals: A study of the effects of surface oxidation. *Physical Review B* **42**, 3164–3166 (1990).
25. Jin, P. Single Crystal VO₂ nanoparticles, Preparation Method and its application. *Japanese Patent JA 2011-178825* (2010).
26. Zhu, C.-L. *et al.* Fe₃O₄/TiO₂ Core/Shell Nanotubes: Synthesis and Magnetic and Electromagnetic Wave Absorption Characteristics. *The Journal of Physical Chemistry C* **114**, 16229–16235 (2010).
27. Demirörs, A. F., van Blaaderen, A. & Imhof, A. A General Method to Coat Colloidal Particles with Titania. *Langmuir* **26**, 9297–9303 (2010).
28. Keddie, J. L., Braun, P. V. & Giannelis, E. P. Interrelationship between Densification, Crystallization, and Chemical Evolution in Sol-Gel Titania Thin Films. *Journal of the American Ceramic Society* **77**, 1592–1596 (1994).
29. Toshikazu, N., Takayuki, Y., Nobuyoshi, M. & Makiko, S. Analysis of firing processes of titania gel films fabricated by sol-gel processes. *Thin Solid Films* **467**, 43–49 (2004).
30. Ding, X.-Z., Qi, Z.-Z. & He, Y.-Z. Effect of hydrolysis water on the preparation of nano-crystalline titania powders via a sol-gel process. *Journal of Materials Science Letters* **14**, 21–22 (1995).
31. Vorkapic, D. & Matsoukas, T. Effect of Temperature and Alcohols in the Preparation of Titania Nanoparticles from Alkoxides. *Journal of the American Ceramic Society* **81**, 2815–2820 (1998).
32. Zhang, S., Kim, I. S. & Lahun, L. J. Stoichiometry Engineering of Monoclinic to Rutile Phase Transition in Suspended Single Crystalline Vanadium Dioxide Nanobeams. *Nano Letters* **11**, 1443–1447 (2011).



33. Keddie, J. L. & Giannelis, E. P. Effect of Heating Rate on the Sintering of Titanium Dioxide Thin Films: Competition between Densification and Crystallization. *Journal of the American Ceramic Society* **74**, 2669–2671 (1991).
34. Yuan, N. Y., Li, J. H. & Lin, C. L. Valence reduction process from sol-gel V₂O₅ to VO₂ thin films. *Appl Surf Sci* **191**, 176–180 (2002).
35. Enomoto, M. The O-Ti-V System (Oxygen-Titanium-Vanadium). *J Phase Equilib* **17**, 539–545 (1996).
36. Golubovic, A. *et al.* Raman study of the variation in anatase structure of TiO₂ nanopowders due to the changes of sol-gel synthesis conditions. *Journal of Sol-Gel Science and Technology* **49**, 311–319 (2009).
37. Jones, A. C., Berweger, S., Wei, J., Cobden, D. & Raschke, M. B. Nano-optical Investigations of the Metal-Insulator Phase Behavior of Individual VO₂ Microcrystals. *Nano Letters* **10**, 1574–1581 (2010).
38. Whittaker, L., Wu, T. L., Patridge, C. J., Sambandamurthy, G. & Banerjee, S. Distinctive finite size effects on the phase diagram and metal-insulator transitions of tungsten-doped vanadium(IV) oxide. *Journal of Materials Chemistry* **21**, 5580–5592 (2011).
39. Tselev, A. *et al.* Interplay between Ferroelastic and Metal-Insulator Phase Transitions in Strained Quasi-Two-Dimensional VO₂ Nanoplatelets. *Nano Letters* **10**, 2003–2011 (2010).
40. Tselev, A. *et al.* Mesoscopic Metal-Insulator Transition at Ferroelastic Domain Walls in VO₂. *Acs Nano* **4**, 4412–4419 (2010).
41. Lee, M.-H. & Kim, M.-G. RTA and stoichiometry effect on the thermochromism of VO₂ thin films. *Thin Solid Films* **286**, 219–222 (1996).
42. Muraoka, Y., Ueda, Y. & Hiroi, Z. Large modification of the metal-insulator transition temperature in strained VO₂ films grown on TiO₂ substrates. In *8th ISSP International Symposium on Correlated Electrons* (ISSP-Kashiwa 2001) 965–967 (Tokyo, Japan; 2001).
43. Du, J. *et al.* Significant changes in phase-transition hysteresis for Ti-doped VO₂ films prepared by polymer-assisted deposition. *Solar Energy Materials and Solar Cells* **95**, 469–475 (2011).
44. Nishikawa, M., Nakajima, T., Kumagai, T., Okutani, T. & Tsuchiya, T. Ti-Doped VO₂ Films Grown on Glass Substrates by Excimer-Laser-Assisted Metal Organic Deposition Process. *Japanese Journal of Applied Physics* **50** (2011). doi: 10.1143/JJAP.50.01BE04
45. Fu, G., Polity, A., Volbers, N. & Meyer, B. K. Annealing effects on VO₂ thin films deposited by reactive sputtering. *Thin Solid Films* **515**, 2519–2522 (2006).
46. Zhang, Z. T., Gao, Y. F., Kang, L. T., Du, J. & Luo, H. J. Effects of a TiO₂ Buffer Layer on Solution-Deposited VO₂ Films: Enhanced Oxidization Durability. *J. Phys. Chem. C* **114**, 22214–22220 (2010).
47. Kucharczyk, D. & Niklewski, T. Accurate X-ray determination of the lattice parameters and the thermal expansion coefficients of VO₂ near the transition temperature. *Journal of Applied Crystallography* **12**, 370–373 (1979).
48. Straumanis, M. E., Ejima, T. & James, W. J. The TiO₂ phase explored by the lattice constant and density method. *Acta Crystallographica* **14**, 493–497 (1961).
49. Cao, J. *et al.* Extended Mapping and Exploration of the Vanadium Dioxide Stress-Temperature Phase Diagram. *Nano Letters* **10**, 2667–2673 (2010).
50. Appavoo, K. *et al.* Role of Defects in the Phase Transition of VO₂ Nanoparticles Probed by Plasmon Resonance Spectroscopy. *Nano Letters* **12**, 780–786 (2012).
51. Kang, M., Kim, S. W., Ryu, J. W. & Noh, T. Optical properties for the Mott transition in VO₂. *AIP Adv.* **2**, 1–6 (2012).
52. Felde, B., Niessner, W., Schalch, D., Scharmann, A. & Werling, M. Plasmon excitation in vanadium dioxide films. *Thin Solid Films* **305**, 61–65 (1997).
53. Plass, G. N. Mie Scattering and Absorption Cross Sections for Absorbing Particles. *Appl. Opt.* **5**, 279–285 (1966).
54. Ben-Messaoud, T. & Landry, G. *et al.* High contrast optical switching in vanadium dioxide thin films. *Opt Commun* **281**, 6024–6027 (2008).
55. Lu, Z., Li, C. & Yin, Y. Synthesis and thermochromic properties of vanadium dioxide colloidal particles. *Journal of Materials Chemistry* **21**, 7 (2011). doi:10.1039/c1jm12430g
56. Wang, C. *et al.* Magnetic (γ -Fe₂O₃@SiO₂)_n@TiO₂ Functional Hybrid Nanoparticles with Activated Photocatalytic Ability. *J. Phys. Chem. C* **113**, 4008–4011 (2009).
57. Xuan, S., Jiang, W., Gong, X., Hu, Y. & Chen, Z. Magnetically Separable Fe₃O₄/TiO₂ Hollow Spheres: Fabrication and Photocatalytic Activity. *The Journal of Physical Chemistry C* **113**, 553–558 (2008).

Acknowledgements

This study was supported in part by a fund from the National Key Basic Research Program (NKBRP, 2009CB939904), the high-tech project of MOST (2012AA030605, 2012BAA10B03), and the National Natural Science Foundation of China (NSFC, Contract No: 51172265, 51032008, 51102270, 51272273, 51272271).

Author contributions

M.K. and Y.M.L. designed the experiment. M.K. did the FESEM and the spectra measurements. Y.M.L. performed synthesis experiments, DSC measuring, photocatalytic evaluation and image analysis. Y.M.L., M.K., S.D.J. and Y.F.G. analysed the data. All authors contributed in writing the paper.

Additional information

Supplementary information accompanies this paper at <http://www.nature.com/scientificreports>

Competing financial interests: The authors declare no competing financial interests.

License: This work is licensed under a Creative Commons Attribution-NonCommercial-NoDerivs 3.0 Unported License. To view a copy of this license, visit <http://creativecommons.org/licenses/by-nc-nd/3.0/>

How to cite this article: Li, Y., Ji, S., Gao, Y., Luo, H. & Kanehira, M. Core-shell VO₂@TiO₂ nanorods that combine thermochromic and photocatalytic properties for application as energy-saving smart coatings. *Sci. Rep.* **3**, 1370; DOI:10.1038/srep01370 (2013).